Ceramics International 48 (2022) 33514–33523

Contents lists available at ScienceDirect

Ceramics International

journal homepage: www.elsevier.com/locate/ceramint

Structure, biocompatibility and corrosion resistance of the ceramic-metal surface of porous nitinol

Ekaterina S. Marchenko [a], Gulsharat A. Baigonakova [a], Yuri F. Yasenchuk [a], Timofey L. Chekalkin [a,b], Alex A. Volinsky [a,c,*]

[a] Laboratory of Superelastic Biointerfaces, National Research Tomsk State University, Tomsk, 634050, Russia
[b] R&D Center, TINIKO, Osong, 28164, Republic of Korea
[c] Department of Mechanical Engineering, University of South Florida, 4202 E. Fowler Ave. ENG 030, Tampa, FL 33620, Tampa, Florida, 33620, USA

ARTICLE INFO

Keywords:
Ceramic-metal surface layer
Self-propagating high-temperature synthesis
Nitinol
Corrosion resistance
Biocompatibility

ABSTRACT

One of the key aspects of the biochemical compatibility of medical alloys is the surface corrosion resistance in living organisms. This study discusses the structure of the ceramic-metal surface layer of a porous nickel-titanium alloy (nitinol) and the corrosion resistance in simulated physiological liquids. The structure of the protective layer and glass-ceramic non-metallic inclusions in the surface of the porous alloy have been studied. The formation of the surface ceramic-metal layer and crystallization of various glass-metal-ceramic phases as a result of chemisorption from reaction gases and epitaxial growth from the gas phase during the self-propagating high-temperature synthesis are observed.

1. Introduction

Porous ceramic and metal materials play an important role in medicine as functional elements in plastic surgery and bone tissue replacement, including biocompatible coatings for implants [1–4]. The porous structure of implants facilitates their biological integration, promotes strong fixation, and ensures unhindered circulation of the biological fluids [5]. Compared with traditional powder metallurgy methods, self-propagating high-temperature synthesis (SHS) has the advantages of producing ceramic and intermetallic compounds due to high efficiency, energy, and time savings [6–8]. Porous NiTi alloy obtained by the SHS method is a promising biomaterial in medicine, the use of which is continuously expanding due to a unique combination of functional properties. Most studies of porous SHS-NiTi are limited to the investigation of pore structure and morphology, along with physical and mechanical characteristics [9–12]. These studies have shown high biomechanical compatibility and fatigue resistance of the porous framework. However, there are no detailed investigations of porous alloys in terms of biochemical compatibility due to the complex analysis of porous framework surfaces that are inhomogeneous in shape, structure, and phase composition. This study is necessary because surface properties, including density, composition, morphology, and surface layer thickness determine the corrosion resistance of implants.

Unlike porous NiTi, the surface properties of dense non-porous alloys have been extensively studied for many years [13–16]. Oxide layers form naturally on the surface of dense Ti and NiTi alloys, consisting mainly of titanium dioxide, which plays a vital role in their biocompatibility and corrosion resistance. This layer effectively passivates the surface under static load conditions, but it is not able to protect the alloy from corrosion under periodic dynamic loads. Therefore, additional surface modifications are carried out to protect titanium-based alloys from corrosion. The corrosion resistance of nitinol and titanium alloys is improved by alloying with Zr, Nb, and Ta elements through the stabilization of surface films in biological fluids by forming ZrO_2, Nb_2O_5, Ta_2O_5, Al_2O_3 ceramic oxides, and/or depositing porous ceramic coatings [17–22]. Introducing Al_2O_3, Nb_2O_5, or NbO_2 oxides into TiO_2 increases surface corrosion resistance. Electrochemical tests have shown that the Al_2O_3 coating prevents active corrosion of the passivated NiTi substrate and acts as an inhibitor [23]. Mg-based coatings can potentially be used for biological NiTi implants due to their biocompatibility with good physical and mechanical properties [24–26]. Li et al. [26] demonstrated that the Mg coatings significantly improved porous Ti_6Al_4V alloys' osteogenesis and osseointegration properties. The research was also carried out regarding the use of various bioactive silicate-based ceramic coatings that enhance the osseointegration and bactericidal properties of metal substrates in biomedical applications [27]. The main

* Corresponding author. Laboratory of Superelastic Biointerfaces, National Research Tomsk State University, Tomsk, 634050, Russia.
E-mail address: volinsky@usf.edu (A.A. Volinsky).

https://doi.org/10.1016/j.ceramint.2022.07.296
Received 16 May 2022; Received in revised form 17 July 2022; Accepted 27 July 2022
Available online 6 August 2022

component used for the production of silicate-based ceramics is wollastonite ($CaSiO_3$). In vitro and in vivo bioactivity, biodegradability, and mechanical properties of $CaSiO_3$ were recently reported by Mohammadi et al. [27]. Bioinert ceramics-metal (cermet) coatings have been widely used to improve the wear and corrosion resistance of titanium-based alloys [28]. The cermet coating' wear resistance is three times higher than the titanium-based substrates and they also have good cytocompatibility. Thus, these studies demonstrate the high corrosion resistance of coatings based on various cermet phases in nickel-titanium alloys. Considering that the reversible austenite-martensite phase transformation gives the porous nickel-titanium alloy the elasticity and endurance inherent to hard body tissues, it is necessary to create a corrosion-resistant metal-ceramic surface that will deform in concert with the porous framework without cracking.

This work aims to create and study cermet layers on the surface of porous SHS-NiTi deformed superelastically up to 6% without failure while demonstrating high corrosion resistance and biocompatibility.

2. Materials and methods

2.1. Preparation of porous NiTi

The porous NiTi alloy is obtained by self-propagating high-temperature synthesis under a special mode of layer-by-layer combustion in an argon atmosphere from a mixture of Ti and Ni powders. Titanium powder with a particle size up to 50 μm was produced by calcium hydride reduction and carbonyl nickel powder had a particle size up to 50 μm. The composition of the powders is listed in Tables 1 and 2.

The powder mixture was placed in a quartz tube (3 cm inner diameter), which was then loaded into a reaction furnace at room temperature. Argon flow was started at 0.05 MPa relative pressure, and then the furnace was heated to 380 °C at a 15 °C/min heating rate. To start the SHS reaction under protective argon gas flow, the powder mixture was ignited by a nichrome filament at 380 °C. The synthesis starting temperature was selected experimentally to obtain a homogeneous isotropic structure and normal pore size distribution. The average pore size is 50–70 μm in Fig. 1.

2.2. Structure characterization methods

The difficult access to the surface of the pores complicates the study of the porous framework. Therefore, the porous alloy was crushed into granules to study the surface structural-phase features. The phase composition and crystallinity of the surfaces of the granules were studied by grazing incidence X-ray phase analysis (GIXRD) at a 1° angle using an XRD-6000 diffractometer with Cu Kα radiation at 40 kV, 40 mA. The data were analyzed using the PDF-4+ database and the POWDER CELL 2.4 full profile analysis software.

Transmission electron microscopy (TEM) studies of the surface layer in the cross-section of thin foils were conducted using a JEOL JEM-2100 microscope (JEOL, Japan). Sample preparation was carried out by ion milling of the SHS-NiTi samples using the EM-09100IS ion slicer cutting and polishing unit (JEOL, Japan).

Scanning electron microscopy (SEM) and optical microscopy focus stacking were used to study the structure of features and inclusions. Using the method of back-scattered electron diffraction, a microstructure map was obtained using field emission scanning electron microscope Tescan MIRA 3 LMU (TESCAN ORSAY HOLDING, Brno, Czech Republic), equipped with Oxford Instruments Ultim Max 40 EDS detector (Oxford Instruments, High Wycombe, UK).

Table 1
Titanium powder composition in at.%.

Ti	N	C	H	Fe	Si	Ca	Cl
Base	0.2	0.05	0.35	0.4	1	0.08	0.004

Table 2
Nickel powder composition in at.%.

Ni	Co	Cu	C	Fe	S
99.8	0.15	0.02	0.03	0.02	0.01

Note: P, Mn, Si, As, Pb, Sb, Bi, Sn, and Zn concentration is below 0.005 at.%.

2.3. Corrosion behavior

The interaction between porous SHS-NiTi alloys and physiological electrolytes was simulated by anodic polarization using a precision potentiostat-galvanostat (P-45X, Electrochemical Instruments, Chernogolovka, Russia) and a standard E−5C three-electrode cell with a graphite counter electrode. Potentiodynamic polarization curves for cylindrical SHS-NiTi samples measuring 29 × 10 mm (diameter × height) were recorded at 37 °C using a standard silver chloride reference electrode (SCE) and three de-aerated electrolytes: 1% HCl, 0.9% NaCl, and PBS buffered to a pH of 7.4 ± 0.2. Tests were conducted retrieving current-voltage characteristics in a linear sweep mode. The potential ranged from −0.7 V to 0.8 V, with the minimum potential determined by the −0.4 V open circuit potential. Such an approach is valid when the surfaces of porous metallic implants are in direct contact with aggressive media in vivo.

Proneness to localized corrosion attack was evaluated according to the ASTM F2129-08. The test included three steps, and it was conducted according to the following procedure: (1) open-circuit potential E_{OCP} measured for 30 min; (2) potentiodynamic test ranging from −50 mV to +50 mV relative to E_{OCP} with a sweep rate of 0.3 mV/s to determine polarization resistance; (3) potentiodynamic test ranging from −400 mV to 1000 mV relative to E_{OCP} with a sweep rate of 0.5 mV/s after E_{OCP} has been preliminarily measured for 5 min. All data were collected using the ES8 software (Electrochemical Instruments, Chernogolovka, Russia) and samples half-immersed in electrolyte solutions.

The specific surface area of the sample was determined using the method of random cross-sections according to the procedure described by Bramfitt et al. [29]. The method is based on the second stereometric ratio:

$$\sum S = \frac{4}{\pi}\sum P = 2m \text{ mm}^{-1} \quad (1)$$

The total surface area per unit volume (specific surface $\sum$S) is equal to the doubled number of intersection points m between random intersecting lines and these surfaces. It is calculated per unit length of the secant as:

$$\sum S = 2m \text{ mm}^2 \Big/ \text{mm}^3 \quad (2)$$

Here, $\sum S$ is the specific surface area in mm^2/mm^3, and m is the average number of intersection points in mm^{-1}. The relationship (2) is valid for any system of spatial surfaces regardless of their shape, location, and orientation. In obtaining equation (2), it was assumed that intersecting lines were randomly oriented in space, and any direction had equal probability. Thus, lines intersecting pore surface boundaries are randomly oriented, and their direction is equiprobable. In our case, the mean value of the specific surface obtained for porous SHS-NiTi samples used to calculate the corrosion parameters related to current density was 5.5 mm^2/mm^3. The polarization resistance *Rp* was calculated from the Stern-Geary equation using the Tafel slopes of the potential-current density curves [30].

2.4. The cytocompatibility study

The cytocompatibility of the surface was assessed using the MCF-7 cell line. This line is widely used for in vitro cytotoxicity studies of the cytocompatibility of various biocompatible materials. MCF-7 cells were

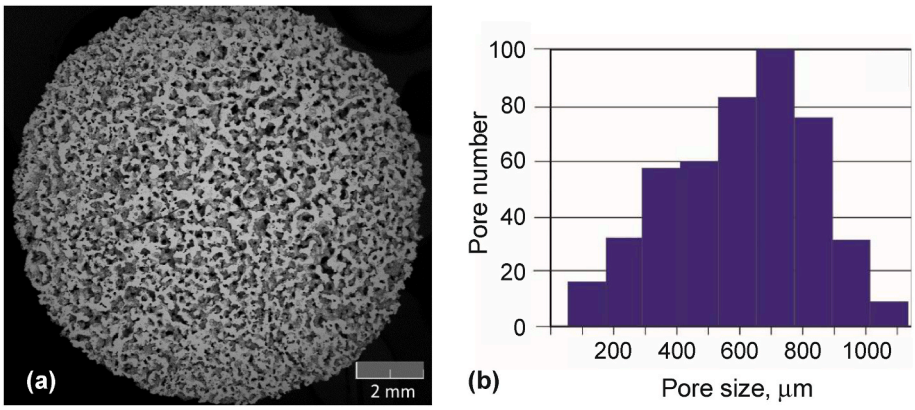

Fig. 1. (a) Macrostructure and (b) pore size distribution histogram of porous NiTi alloy obtained by the SHS method.

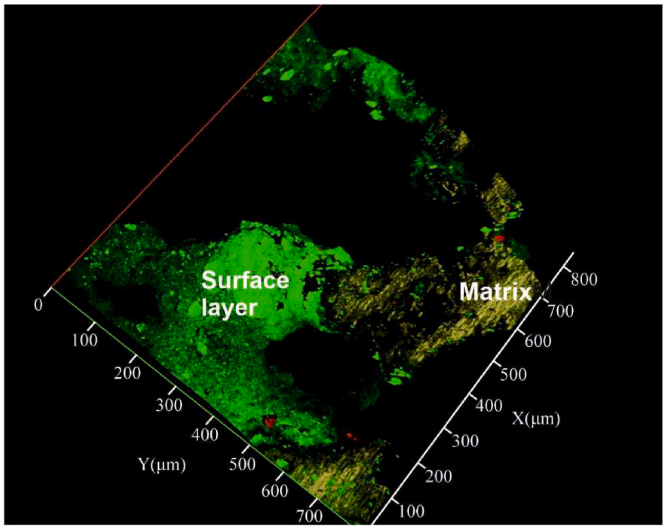

Fig. 2. Scanning confocal microscopy image of the porous NiTi thin section surface.

incubated for 24 h on a porous SHS-NiTi surface and evaluated by the 3-(4,5-dimethylthiazol-2-yl)-2,5-diphenyl tetrazolium bromide (MTT) analysis in static cultivation. The fluorescence of the samples from the 10 × 10 mm^2 surface areas was visualized using the LSM-750 confocal laser scanning microscope (Carl Zeiss, Germany). Cells were visualized using double staining where living cells were stained with acridine orange and dead cells with ethidium bromide. The fluorescence of acridine orange was excited by a 488 nm wavelength laser, and the fluorescence was recorded in the 495–545 nm range. The fluorescence of ethidium bromide was excited by a 561 nm wavelength laser, and the fluorescence was recorded in the 580–690 nm range. The result was an overlay image of green acridine orange fluorescence and ethidium bromide red fluorescence obtained in the transmitted light mode.

3. Results and discussion

3.1. Structure and phase composition of the porous SHS-NiTi matrix and surface layer

A layer firmly bound to the matrix is formed on the surface of the porous framework during the SHS reaction. Impurities dissolved and adsorbed in reactants, along with synthesis reaction gases of the protective atmosphere form this surface layer. The surface layer is green in the confocal scanning microscopy image, while the polished matrix is brown in Fig. 2.

3.1.1. Porous NiTi alloy matrix

Scanning electron microscopy has established that the matrix of the porous alloy consists of the NiTi solid solution grains, intergranular peritectic Ti_2Ni phase, and Ti_2Ni secondary phase particles in Fig. 3. Using the method of back-scattered electron diffraction, crystal orientation maps were obtained for the porous SHS-NiTi sample in Fig. 4. The matrix contains randomly distributed equiaxed grains 5–20 μm in diameter. EBSD results showed that the Ti_2Ni peritectic phase size varies from 0.5 μm to 2 μm. The inverse pole figure (IPF) maps demonstrate the presence of intragrain high-angle boundaries with >15° misorientation angles. In all projections, a more homogeneous internal structure of the grains was found. Only some grains have domain structures with non-equiaxed orientations.

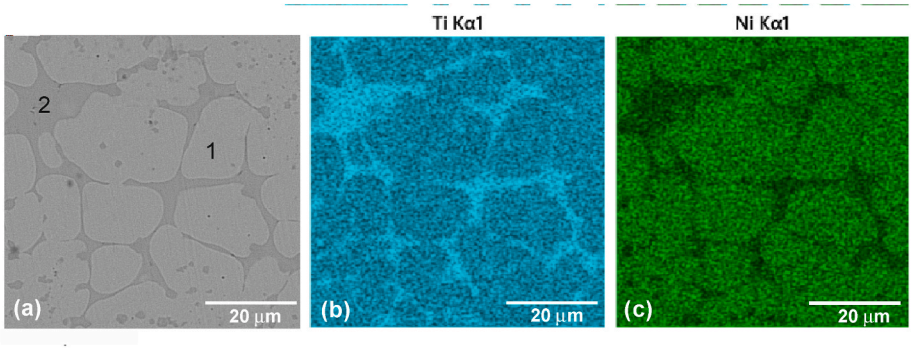

Fig. 3. (a) Microstructure and distribution maps of (b) titanium and (c) nickel in porous NiTi alloy. Here, 1 - TiNi and 2 - Ti_2Ni.

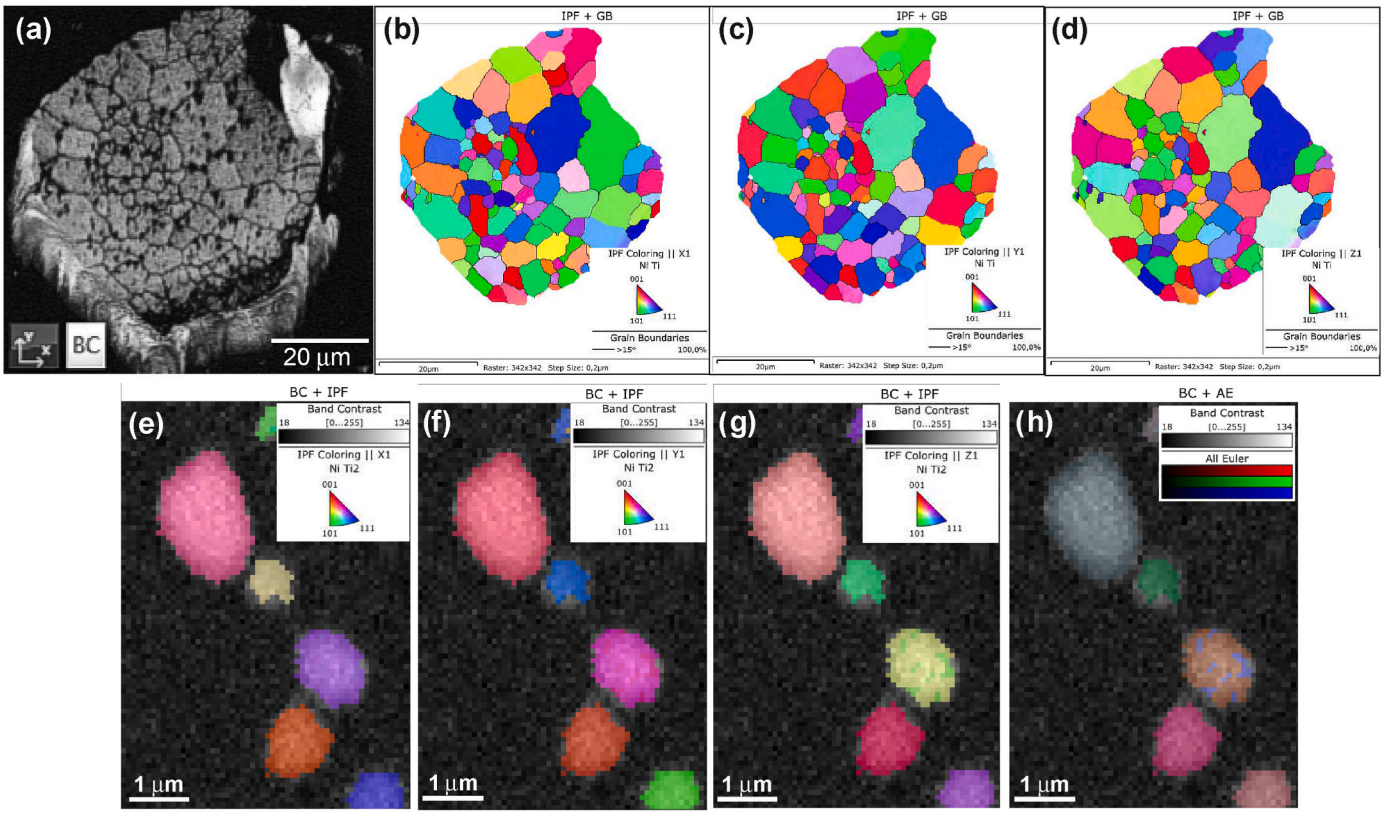

Fig. 4. (a) SEM image and crystal orientation maps obtained for the TiNi phase and (b) X, (c) Y, (d) Z direction inverse pole figure color orientation maps of TiNi phase and (e) X, (f) Y, (g) Z direction inverse pole figure color crystal orientation maps obtained for the Ti_2Ni.

Pole figures were constructed for the (100), (110), and (111) planes, where the density isolines indicate the presence of the grains' crystallographic preferred orientation in Fig. 5. The presence of multiple high-intensity randomly located sharp reflections indicates the crystallographic mechanisms of texture formation and the appearance of recrystallized grains. The maximum pole density was recorded for the (001) crystals in the X direction and (111) in the Y direction. The direct pole figures show higher intensity reflections for the {100} planes in the X direction and insignificant lower intensity reflections for the {111} planes in the Z direction.

3.1.2. *Surface layer of porous SHS-NiTi alloy*

The surface layer of the porous NiTi sample was studied by structural characterization methods. Transmission electron microscopy (TEM) studies of the surface in cross-section showed that the surface layer consists of the lower (2) and upper (3) layers in Fig. 6. The diffraction patterns taken from the layers identified the $Ti_4Ni_2O(N,C)$ intermetallic compound, differing in the degree of crystallinity. The complex structure of the surface layer is associated with the convective transfer of gasified impurities and melt from the reaction zone. Presumably, the amorphous loose upper layer is formed due to the capture of the melted part by the reaction gases and the transfer of impurities in the aerosol form. A continuous amorphous-nanocrystalline lower layer is formed by the chemoepitaxial mechanism in two stages. In the first stage, as a result of the chemisorption of O, N, and C impurities from the reaction gases, an amorphous Ti–Ni–C–N–O film is formed on the surface of the peritectic liquid. As a result of the amorphous Ti–Ni–C–N–O film crystallization, the epitaxial growth of the nanocrystalline $Ti_4Ni_2O(N,C)$ cermet phase occurs in the second stage. The process of the surface layer formation is discussed in detail in the next subsection.

X-ray diffraction (XRD) studies of the granules' surface have revealed the presence of X-ray amorphous and crystalline $Ti_4Ni_2O(N,C)$ phases in Fig. 7. Amorphous structure in X-ray diffractograms is characterized by an amorphous halo in the $2\theta < 30^\circ$ initial diffraction angle region, which is consistent with the diffuse halo in the TEM diffraction pattern. The intermetallic nanocrystalline oxycarbonitride $Ti_4Ni_2O(N,C)$ is the main phase of the surface layers. In addition, the XRD diffractograms revealed the presence of glass- and metal-ceramic phases of various compositions: $CaSiO_3$, and $MgAl_2O_4$ (up to 20 vol%). The broadened low-intensity diffraction reflections of the $Ti_4Ni_2O(N,C)$ phase indicate its small crystallite size. Also, phase reflections of the matrix based on the NiTi compound with the austenitic structure were revealed.

According to the energy dispersive spectra (EDS) analysis of the porous NiTi interpore bridges, an increase in O, C, and N interstitial impurities concentration in the surface layer is observed. This is consistent with the XRD data and confirms the presence of the $Ti_4Ni_2O(N,C)$ intermetallic oxycarbonitride surface layer in Fig. 8.

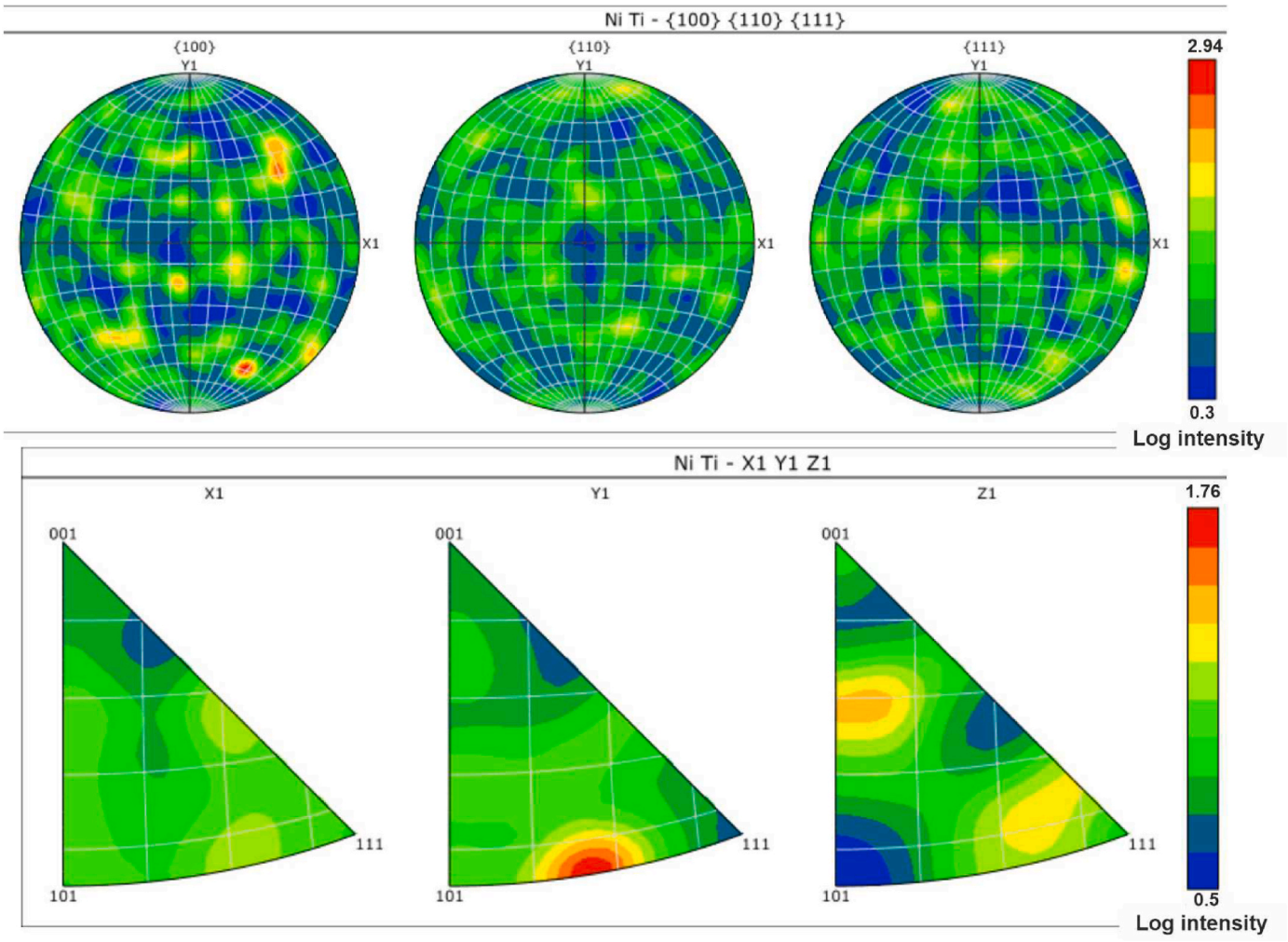

Fig. 5. (100), (110), and (111) pole figures for the TiNi phase.

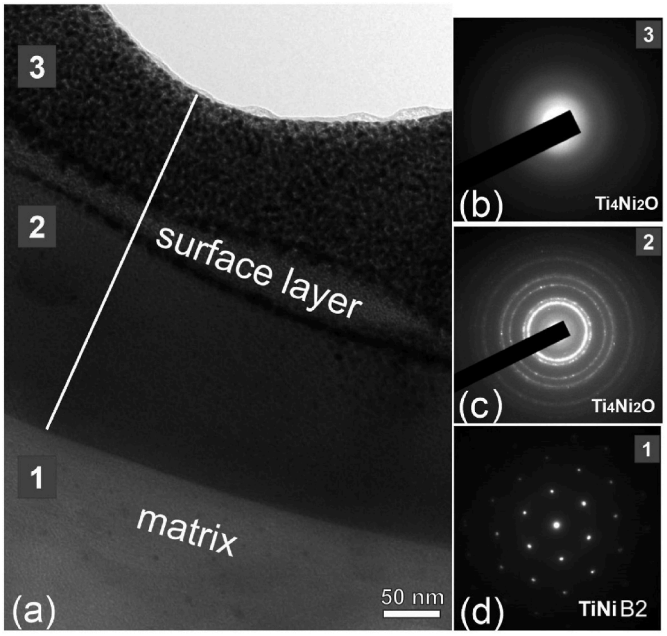

Fig. 6. (a) TEM image of the porous NiTi alloy surface cross-section with corresponding diffraction patterns of (b) the upper surface layer 3, (c) the lower surface layer 2, (d) the matrix 1.

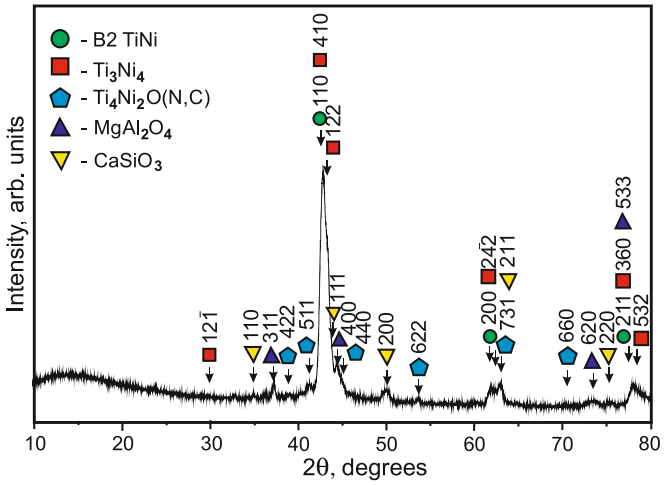

Fig. 7. X-ray diffraction pattern of the porous NiTi granules.

3.2. Schematic description of the surface cermet layer formation

To explain the process of the surface cermet layer formation in the layer-by-layer combustion mode, a schematic description is presented in Fig. 9. At the initial stage, a eutectic liquid is formed during the contact melting of the powder mixture reactants. The beginning of an

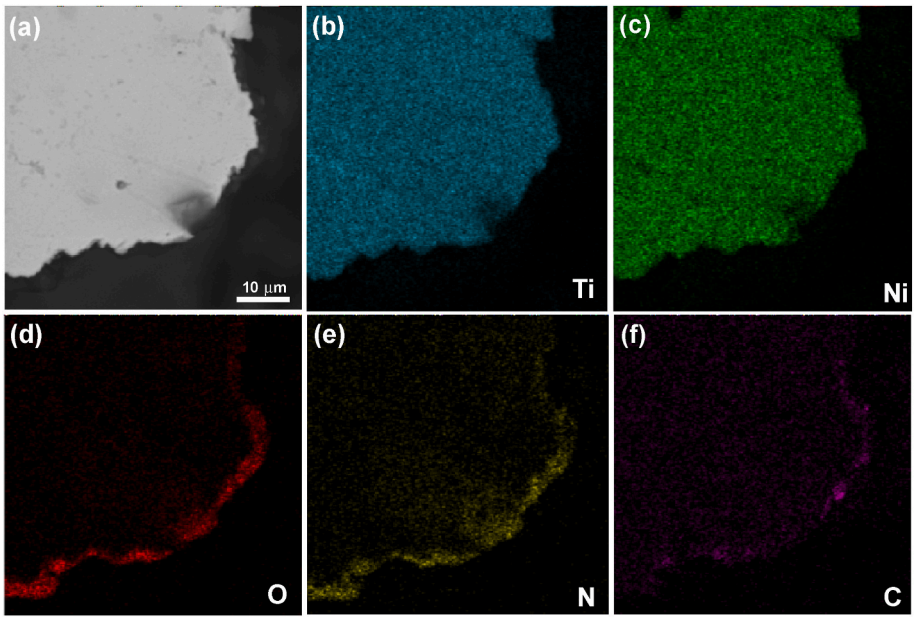

Fig. 8. Energy-dispersive analysis of the interpore bridge of porous NiTi alloy: (a) SEM image, and (b) Ti, (c) Ni, (d) O, (e) N, and (f) C maps.

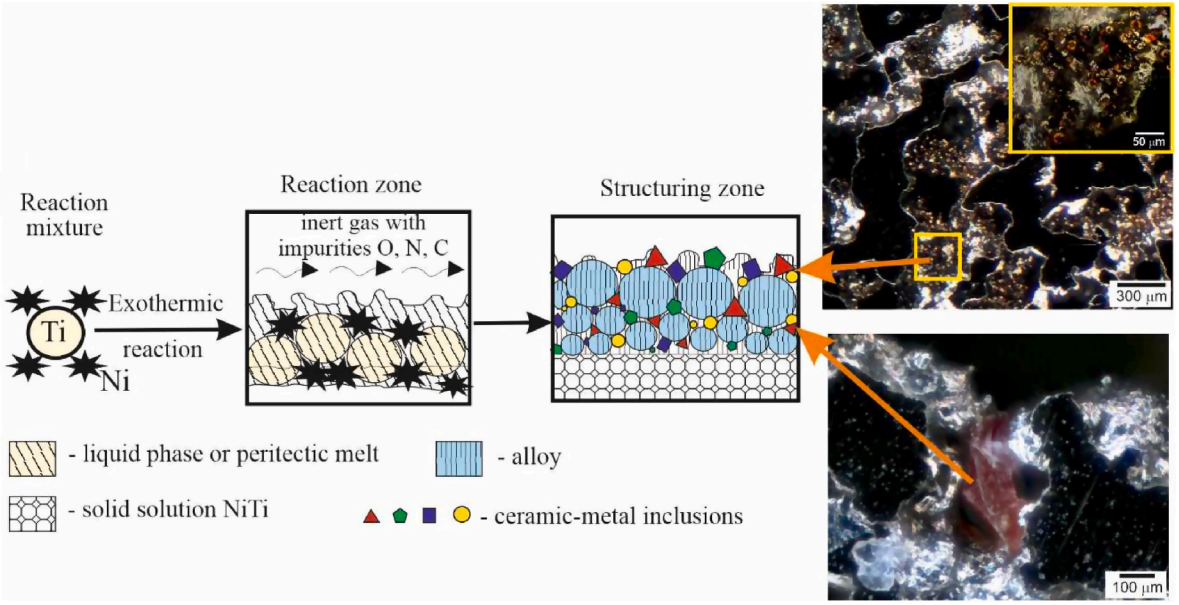

Fig. 9. Schematics of the surface cermet layer formation.

exothermic reaction between nickel and titanium is associated with heating the reaction products and is partially dissipated by the emission of the melt products and reaction gases from the reaction zone. The reaction occurs in the self-propagation mode, capturing new areas of the heating zone by wetting titanium and nickel particles with a eutectic melt. As a result, a new intermetallic TiNi phase is synthesized. Thus, the reaction zone for the synthesis of the NiTi intermetallic compound moves through the powder mixture due to heat and mass transfer, which is carried out by wetting, capillary spreading of the eutectic liquid, and convective transfer of heat and peritectic melt by a mixture of reaction gases of the argon atmosphere.

After the completion of the main exothermic synthesis of the NiTi intermetallic compound, the final formation of the structure occurs in the peritectic reaction (Liquid + TiNi═Ti_2Ni + TiNi), which occurs at the NiTi grain boundaries. The peritectic melt layer formed in the reaction zone around the NiTi grains has a composition close to the stoichiometry of the Ti_2Ni constituent. The surface layer of the peritectic Ti_2Ni melt, interacting with the reaction gases, is saturated with interstitial oxygen, nitrogen, and carbon impurities. Therefore, the crystallized layers are intermetallic oxycarbonitrides $Ti_4Ni_2O(N,C)$. Chemisorption of gaseous interstitial impurities by the peritectic layer leads to the formation of a dense oxycarbonitride nanolayer. In this case, the gas condensate formed in the reaction zone from gasified impurities and melt is carried by the reaction gases along with the formed porous framework. Gas condensation on the peritectic melt film that conceals the metallic framework leads to the selective crystallization of new non-metallic inclusions in the form of crystals and spherical formations on the surface.

Multiple spherical inclusions are located on the surface of open pores in Fig. 10(a). The spherical inclusions have a complex structure, where

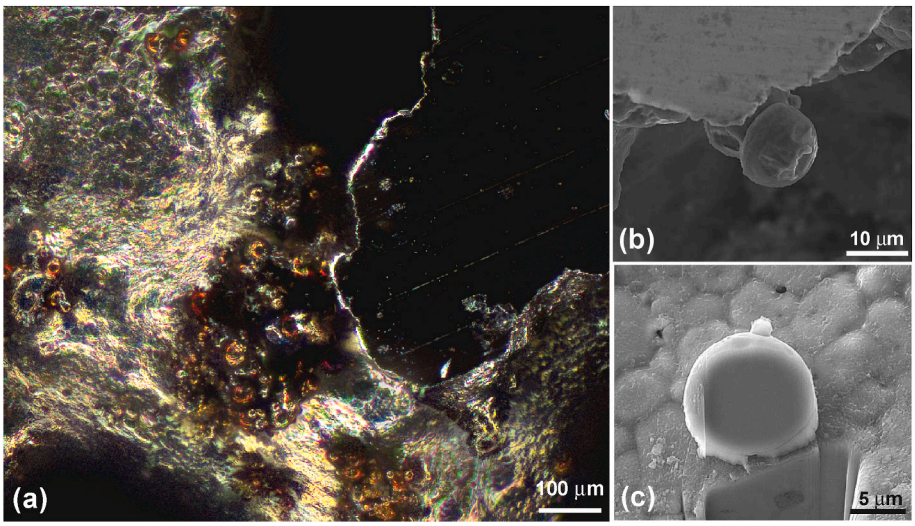

Fig. 10. (a) Optical image of spherical inclusions and (b) SEM image of a spherical inclusion on the surface of porous SHS-NiTi; (c) inclusion cross-section.

Table 3
Chemical composition of two spherical inclusions in at.% obtained by EDS.

Spherical inclusion	C	N	O	Mg	Al	Si	P	S	Ca	Ti	Ni
1	16.15	4.77	14.44	0.44	0.76	0.76	0.74	0.24	0.26	34.43	27.01
2	25.53	4.21	12.63	0.43	0.64	0.66	0.46	0.2	0.56	30.08	24.59

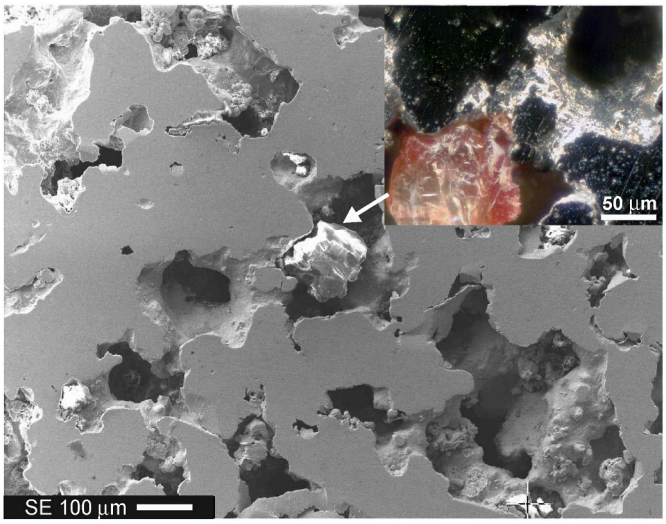

Fig. 11. SEM and stacked optical images of crystalline inclusions on the surface of the porous SHS-NiTi.

the core is a non-metallic inclusion covered with a spherical shell due to condensation of the reaction gases in Fig. 10(b and c). The elemental composition of spherical inclusions was determined by EDS. The EDS analysis showed the presence of Ti, Ni, Si, S, Ca, O, and N elements in a spherical inclusion in Fig. 10(c), with the composition summarized in Table 3. The Ti, Ni, Si, Al, Ca, Mg, P, S, O, N, and C elements were found in other spherical inclusions, indicating the formation of a glass-ceramic compound.

Large crystalline inclusions are present in the NiTi pores (Fig. 11). The uneven faceted surface morphology of these 50–100 μm crystals did not allow obtaining reliable chemical composition results. However, EDS mapping of the porous framework walls with crystalline inclusions has shown that they contain Si, Al, K, and O elements. Presumably, these are $AlSiO_4$ and $KAlSiO_4$ aluminosilicates, along with SiO_2 and CaO oxides in Fig. 12.

Thus, in addition to the formation of intermetallic NiTi phases, titanium-rich Ti_2Ni and nickel-rich Ti50-xNi50+x constituents, new non-metallic spherical and crystalline phases are synthesized from thermally dissociated O, N, C, Al, Ca, Si, Mg, K, Na, Cl, S, and P impurities in the reaction zone. Ceramic inclusions formed in the liquid eutectic phase before the NiTi synthesis ended completely. The reason for this phenomenon is that the crystallization temperature of glass-ceramics is higher than that of the near-equiatomic NiTi constituents. Some already solidified non-metallic inclusions moved during NiTi alloy structuring and coalescence of pores without immersing in the NiTi matrix. At the same time, ceramic inclusions were formed from trapped impurities which are thermally dissociated from reactants.

3.3. Cytocompatibility of the NiTi porous alloy surface

Fig. 13 shows morphological images of MCF-7 cells on the porous SHS-NiTi alloy at low and high magnification. These cells demonstrate viability upon contact with the surface of porous NiTi samples. Confocal laser scanning microscopy was performed 72 h after cultivation with MCF-7 cells. Local surface areas cultivated with MCF-7 cells were found on the sample, where live cells are seen in green with red nuclei. The MTT test has revealed a low 14 ± 7% level of cytotoxicity toward MCF-7 cells. Confocal laser scanning microscopy images show that green cells attached to the surface of the SHS-NiTi extend over the entire sample in Fig. 13(a). The cells are evenly distributed on the surface and to a greater extent inhabit the entire upper surface of the sample. The cells show numerous cytoplasmic structures and many of them have a proliferative morphology in Fig. 13(b).

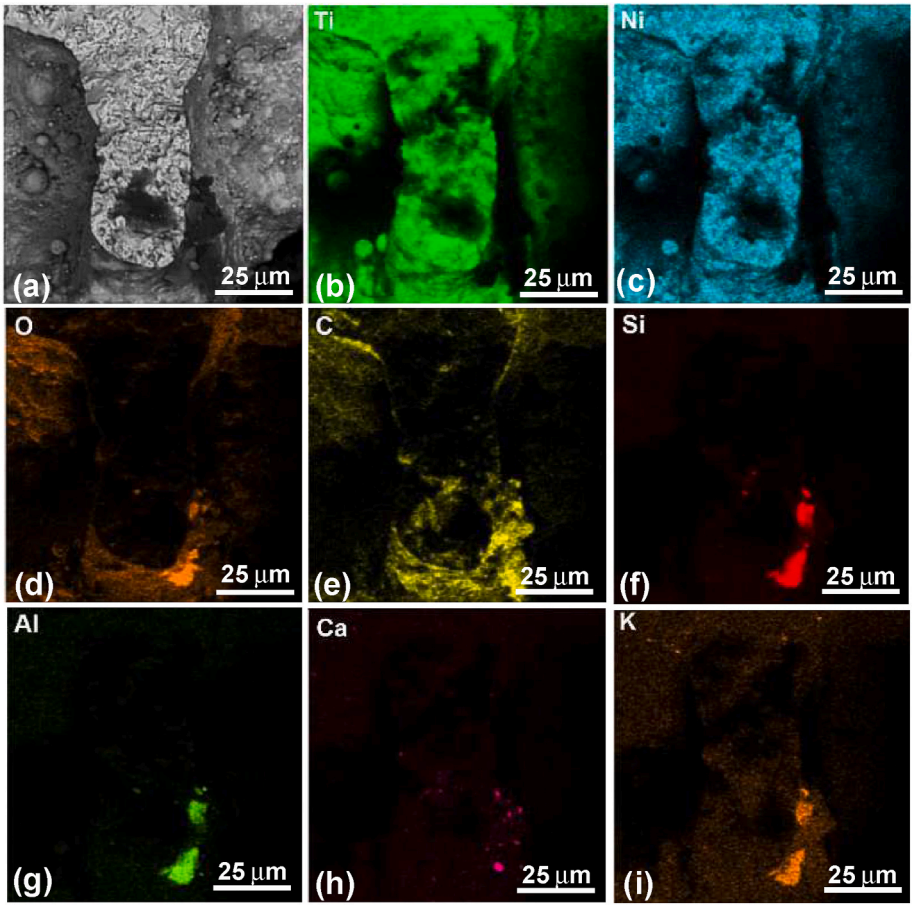

Fig. 12. (a) SEM image and EDS maps of interpore bridge with crystalline inclusions: (b) Ti, (c) Ni, (d) O, (e) C, (f) Si, (g) Al, (h) Ca and (i) K maps.

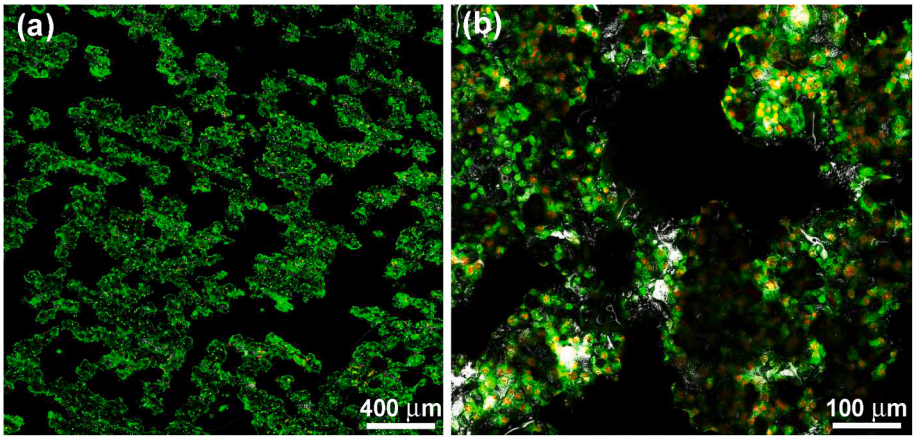

Fig. 13. Confocal laser scanning microscopy image of MCF-7 cells on the SHS-NiTi porous alloy: (a) lower and (b) higher magnification.

3.4. Susceptibility to localized corrosion

Corrosion test results are summarized in Table 4 and Fig. 14. Tafel curves in Fig. 14 demonstrate the potentiodynamic polarization behavior of porous SHS-NiTi samples in different electrolytes at 37 °C. There is an obvious similarity of polarization curves in terms of the dependence of the current density on the studied samples' surface *lg*I (A/cm^2) on the changing potential U (mV). The obtained polarization curves consist of two parts. The first cathodic part (monotonic from −400 mV) refers to the desorption of oxygen adsorbed by the surface. The second anodic part in the form of an inverse parabola from −205

Table 4
Potentiodynamic polarization parameters of porous SHS-NiTi in physiological electrolytes at 37 °C.

Electrolyte	U_{cor}, mV	i_{cor}, μA	R_p, kΩ
PBS	−136.5	1.12	342
NaCl	−186	1.37	258
HCl	−205	1.58	224

Note: U_{cor} - corrosion potential; i_{cor} - corrosion current; *Rp* - polarization resistance.

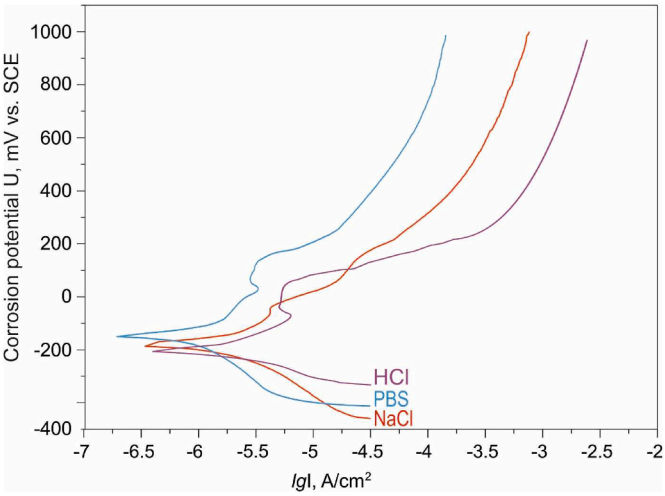

Fig. 14. Potentiodynamic curves of porous SHS-NiTi in physiological electrolytes at 37 °C.

mV to −136 mV corresponds to the hydrogen evolution reaction. According to the data, the lowest corrosion potential U_{cor} is observed in the aqueous hydrochloride solution. The surface corrosion current density is minimum in phosphate-buffered saline (PBS) solution and maximum in HCl solution. The highest polarization resistance of 342 kΩ was measured in PBS, and it is more than one and a half times higher than 224 kΩ in HCl.

The data published in the literature indicate that if the corrosion potential of Ti-based alloys varies from +100 mV to −200 mV compared to the saturated calomel electrode (SCE), the material can be considered conditionally passive or corrosion-proof [31,32]. At the same time, when the corrosion potential is between −200 mV and −450 mV, moderate pitting corrosion can occur. The corrosion-prone behavior is observed from −450 mV to −600 mV corrosion potential. A comparative analysis of susceptibility to localized corrosion of porous SHS-NiTi in physiological electrolytes is indicative of a stationary corrosion potential relative to the reference electrode potential that varies from −130 mV to −205 mV. This fact attests to the ennobling effect of the surface film on in vivo electrochemical characteristics, including the oxycarbonitride superficial layer concealing the intermetallic matrix, which is an inherent attribute of the SHS reaction [33,34]. Considering the qualitative resemblance of the anodic curves with those reported for wrought nitinol [35], it might be argued that negligible oxidation of the Ti constituent contained in the surface film occurs with the subsequent formation and growth of the passivating titanium dioxide (rutile) layer. In so doing, the latter can be modestly dissolved at higher values of polarization potential. This indicates that the oxycarbonitride multifarious stratum reliably inhibits the corrosion process, without its meaningful oxidation-induced reaction or dissociation when a porous SHS-NiTi implant is chemically attacked in vivo.

Comparatively, dense nitinol-based alloys demonstrate a clear and predictable corrosion behavior, whereas that of porous SHS-NiTi seems to be tangled since elucidating the corrosion performance of porous SHS-NiTi is an ambitious and challenging undertaking due to the variety of factors including the developed specific surface and structural heterogeneity. Quantification of electrochemical corrosion parameters for each porous sample and analyzing the Tafel curves are also lengthy and time-consuming tasks because the automated processing of the obtained curves in different electrolytes does not allow their unambiguous interpretation. Despite the seeming similarity in the shape of polarization curves, the existing scatter of the obtained corrosion parameters is obviously due to the heterogeneity and complex structural morphology of the studied samples, which can be indicative of local foci of pitting corrosion. Similar difficulties and controversial interpretations have been previously reported in the literature [36–40]. The role of potential distribution inside the pore and porous structure in the electrochemical corrosion behavior of porous NiTi is an important factor. The potential distribution plays the role that strengthens the differences among the various parts of the porous metal surface. This is the crucial electrochemical condition that may even lead to localized corrosion, as reported for porous NiTi-based alloys obtained by other powder metallurgy methods [38,39]. A quantitative method of prolonged exposure to electrolyte solutions and weighing samples is believed to be more reliable and accurate. Moreover, to increase the potential and durability of biomedical devices made of porous SHS-NiTi alloys, it is very important to study and compare the proneness to localized corrosion in porous SHS-NiTi samples subjected to high-temperature atmospheric oxidation [41–43].

In summary, our findings suggest that anodic polarization of porous SHS-NiTi produces a passive film superior to dense NiTi-based intermetallics or Ti medical-grade alloys. Samples were instantaneously re-passivated with a protection potential higher than the corrosion potential. Corrosion-electrochemical activation of porous SHS-NiTi materials is very unlikely in the context of biomedical devices made of these alloys, which excludes reaching high positive potentials in vivo including risks of galvanic pairs.

4. Conclusions

The biochemical compatibility of porous nitinol obtained by the SHS method has been studied experimentally. The bioinertness of the porous alloy surface is due to a corrosion-resistant cermet surface layer, which is a hallmark of the SHS reaction and does not require additional surface modifications. Based on the experimental studies, the following conclusions are summarized.

1. It was found that the surface layer consists of the lower dense and upper sparse layers. The lower dense layer with a thickness of not more than 100 nm has a dense amorphous-nanocrystalline structure of intermetallic oxycarbonitrides firmly bonded to the matrix. The upper 25–300 nm cermets phases form a thick sparse amorphous layer with complex composition. It consists of glass-ceramic crystals, spinels, and silicates of various shapes, sizes, and elemental compositions.
2. XRD analysis demonstrated that the main phase of the surface layers of porous NiTi alloys is the nanocrystalline $Ti_4Ni_2O(N,C)$ oxycarbonitride. The presence of $CaSiO_3$, $MgAl_2O_4$, $AlSiO_4$, $KAlSiO_4$, SiO_2, and CaO ceramic-metal crystal groups with up to 20% volume fraction has been revealed in the surface layers.
3. The formation mechanisms of the cermet surface layer and nonmetallic phases were identified based on the XRD, optical microscopy, SEM, TEM, and EDS results, following the existing SHS model. It has been suggested that the surface layer is formed with the participation of impurities, dissolved and adsorbed in titanium and nickel powders, and reaction gases of the protective atmosphere in which the synthesis is carried out. Inclusions are formed by selective condensation from reaction gases in a peritectic melt from dissociated impurities inherited from powders.
4. From the anodic polarization, the high corrosion resistance of porous NiTi made by the SHS method has been experimentally proven. Porous SHS-NiTi is less prone to localized corrosion compared with wrought NiTi or porous NiTi alloys made by other powder metallurgy methods. The surface multiphase cermet layer reliably isolates the metal matrix of the alloy from the electrochemical effects of biological fluids in vivo. The obtained results confirmed that porous SHS-NiTi meets the criteria of corrosion resistance for materials designed for biomedical applications.
5. High viability and proliferative activity of cells on the surface of porous SHS-NiTi were shown. Corrosion resistance and biocompatibility of the cermet surface of the porous alloy make it possible to

effectively use SHS-NiTi as an implant material for bone grafting and scaffolding.

Declaration of competing interest

The authors declare that they have no known competing financial interests or personal relationships that could have appeared to influence the work reported in this paper.

Acknowledgments

This research was supported by the Mega grant from the Government of the Russian Federation No. 220 of April 09, 2010 (Agreement No. 075-15-2021-612 of June 04, 2021). The research was carried out using the equipment of the Tomsk Regional Core Shared Research Facilities Center of the National Research Tomsk State University, supported by the grant of the Ministry of Science and Higher Education of the Russian Federation 075-15-2021-693 (No. 13.RFC.21.0012).

References

[1] M. Bram, T. Ebel, M. Wolff, A.P. Cysne Barbosa, N. Tuncer, in: I. Chang, Y. Zhao (Eds.), Woodhead Publishing Series in Metals and Surface Engineering, Advances in Powder Metallurgy, Woodhead Publishing, Cambridge, 2013, pp. 520–554.

[2] I.N. Popescu, R. Vidu, V. Bratu, Porous metallic biomaterials processing (review) Part 1: compaction, sintering behavior, properties and medical applications, Sci. Bull. Valahia Univ. Mater. Mech. 15 (2017) 28–40, https://doi.org/10.1515/bsmm-2017-0015.

[3] R. Sarkar, G. Banerjee, Ceramic based bio-medical implants, Interceram 59 (2010) 98–102.

[4] S. Balasubramanian, B. Gurumurthy, A. Balasubramanian, Biomedical applications of ceramic nanomaterials: a review, Int. J. Pharm. Sci. Res. 8 (2017) 4950–4959, https://doi.org/10.13040/ijpsr.0975-8232.8(12).4950-59.

[5] Y.-H. Li, L. Rong, Y. Li, Pore characteristics of porous NiTi alloy fabricated by combustion synthesis, J. Alloys Compd. 325 (2001) 259–262, https://doi.org/10.1016/S0925-8388(01)01382-2.

[6] B.Y. Li, L.J. Rong, Y.Y. Li, V.E. Gjunter, Synthesis of porous Ni-Ti shape-memory alloys by self-propagating high-temperature synthesis: reaction mechanism and anisotropy in pore structure, Acta Mater. 48 (2000) 3895–3904, https://doi.org/10.1016/S1359-6454(00)00184-1.

[7] A.G. Merzhanov, History and recent developments in SHS, Ceram. Int. 21 (1995) 371–379, https://doi.org/10.1016/0272-8842(95)96211-7.

[8] S.D. Dunmead, D.W. Readey, C.E. Semler, J.B. Hol, Kinetics of combustion synthesis in the Ti-C and Ti-C-Ni Systems, J. Am. Ceram. Soc. 72 (12) (1989) 2318–2324.

[9] C.A. Biffi, P. Bassani, Z. Sajedi, P. Giuliani, A. Tuissi, Laser ignition in self-propagating high temperature synthesis of porous nitinol shape memory alloy, Mater. Lett. 193 (2017) 54–57, https://doi.org/10.1016/j.matlet.2017.01.097.

[10] P. Bassani, S. Panseri, A. Ruffini, M. Montesi, M. Ghetti, C. Zanotti, A. Tampieri, A. Tuissi, Porous NiTi shape memory alloys produced by SHS: Microstructure and biocompatibility in comparison with Ti_2Ni and $TiNi_3$, J. Mater. Sci. Mater. Med. 25 (2014) 2277–2285, https://doi.org/10.1007/s10856-014-5253-x.

[11] G. Tosun, N. Orhan, L. Özler, Investigation of combustion channel in fabrication of porous NiTi alloy implants by SHS, Mater. Lett. 66 (2012) 138–140, https://doi.org/10.1016/j.matlet.2011.08.023.

[12] N. Resnina, V. Rubanik Jr., V. Rubanik, M. Kulak, S. Belyaev, P. Liulchak, D. Chepela, V. Kalganov, Influence of the Ar pressure on the structure of the NiTi foams produced by self-propagating high-temperature synthesis, Mater. Lett. 299 (2021), 130047, https://doi.org/10.1016/j.matlet.2021.130047.

[13] B. Yuan, X.P. Zhang, M. Zhu, M.Q. Zeng, C.Y. Chung, A comparative study of the porous TiNi shape-memory alloys fabricated by three different processes, Metall. Mater. Trans. A 37 (2006) 755–761, https://doi.org/10.1007/s11661-006-0047-5.

[14] L. Mohan, C. Anandan, N. Rajendran, Electrochemical behavior and bioactivity of self-organized TiO_2 nanotube arrays on Ti-6Al-4V in Hanks' solution for biomedical applications, Electrochim. Acta 155 (2015) 411–420, https://doi.org/10.1016/j.electacta.2014.12.032.

[15] N.A. Al-Mobarak, A.A. Al-Swayih, Development of titanium surgery implants for improving osseointegration through formation of a titanium nanotube layer, Int. J. Electrochem. Sci. 9 (2014) 32–45.

[16] M. Geetha, A.K. Singh, R. Asokamani, A.K. Gogia, Ti based biomaterials, the ultimate choice for orthopaedic implants - a review, Prog. Mater. Sci. 54 (2009) 397–425, https://doi.org/10.1016/j.pmatsci.2008.06.004.

[17] L. Zhang, L. Chen, A review on biomedical titanium alloys: recent progress and prospect, Adv. Eng. Mater. 21 (2019), 1801215, https://doi.org/10.1002/adem.201801215.

[18] W.Y. Guo, J. Sun, J.S. Wu, Electrochemical and XPS studies of corrosion behavior of Ti-23Nb-0.7Ta-2Zr-O alloy in Ringer's solution, Mater. Chem. Phys. 113 (2009) 816–820, https://doi.org/10.1016/j.matchemphys.2008.08.043.

[19] K.A. Shukla, R. Balasubramaniam, Effect of surface treatment on electrochemical behavior of CP Ti, Ti-6Al-4V and Ti-13Nb-13Zr alloys in simulated human body fluid, Corrosion Sci. 48 (2006) 1696–1720, https://doi.org/10.1016/j.corsci.2005.06.003.

[20] Y.L. Zhou, M. Niinomi, T. Akahori, H. Fukui, H. Toda, Corrosion resistance and biocompatibility of Ti-Ta alloys for biomedical applications, Mater. Sci. Eng. 398 (2005) 28–36, https://doi.org/10.1016/j.msea.2005.03.032.

[21] M. Rüger, T.J. Gensior, C. Herren, M. von Walter, C. Ocklenburg, R. Marx, H.J. Erli, The removal of Al_2O_3 particles from grit-blasted titanium implant surfaces: effects on biocompatibility, osseointegration and interface strength in vivo, Acta Biomater. 6 (2010) 2852–2861, https://doi.org/10.1016/j.actbio.2010.01.009.

[22] I. Milošev, T. Kosec, H.H. Strehblow, XPS and EIS study of the passive film formed on orthopaedic Ti-6Al-7Nb alloy in Hank's physiological solution, Electrochim. Acta 53 (2008) 3547–3558, https://doi.org/10.1016/j.electacta.2007.12.041.

[23] C.C. Kei, Y.S. Yu, J. Racek, D. Vokoun, P. Sittner, Atomic layer-deposited Al_2O_3 coatings on NiTi alloy, J. Mater. Eng. Perform. 23 (2014) 2641–2649, https://doi.org/10.1007/s11665-014-0956-1.

[24] N.A. Agha, R. Willumeit-Römer, D. Laipple, B. Luthringer, F. Feyerabend, The degradation interface of magnesium based alloys in direct contact with human primary osteoblast cells, PLoS One 11 (2016), e0157874, https://doi.org/10.1371/journal.pone.0157874.

[25] W. Ding, Opportunities and challenges for the biodegradable magnesium alloys as next-generation biomaterials, Regen. Biomater. 3 (2016) 79–86, https://doi.org/10.1093/rb/rbw003.

[26] X. Li, P. Gao, P. Wan, Y. Pei, L. Shi, B. Fan, C. Shen, X. Xiao, K. Yang, Z. Guo, Novel bio-functional magnesium coating on porous Ti6Al4V orthopaedic implants: in vitro and in vivo study, Sci. Rep. 7 (2017), 40755, https://doi.org/10.1038/srep40755.

[27] H. Mohammadi, N. Muhamad, A.B. Sulong, M. Ahmadipour, Recent advances on biofunctionalization of metallic substrate using ceramic coating: how far are we from clinically stable implant? J. Taiwan Inst. Chem. Eng. 118 (2021) 254–270, https://doi.org/10.1016/j.jtice.2021.01.013.

[28] T. Chen, Z. Deng, D. Liu, X. Zhu, Y. Xiong, Bioinert TiC ceramic coating prepared by laser cladding: microstructures, wear resistance, and cytocompatibility of the coating, Surf. Coat. Technol. 423 (2021), 127635, https://doi.org/10.1016/j.surfcoat.2021.127635.

[29] B.L. Bramfitt, A.O. Benscoter, Metallographer's Guide: Practices and Procedures for Irons and Steels, first ed., ASM International, Ohio, 2002.

[30] M. Stern, A.L. Geaby, Electrochemical polarization, J. Electrochem. Soc. 104 (1957) 56–63, https://doi.org/10.1149/1.2428496.

[31] F. Ionescu, L. Reclaru, L.C. Ardelean, A. Blatter, Comparative analysis of the corrosion resistance of titanium alloys intended to come into direct or prolonged contact with live tissues, Mater 12 (2019) 2841–2868, 10.3390/ma12172841.

[32] I. Milošev, B. Kapun, The corrosion resistance of nitinol alloy in simulated physiological solutions. Part 1: the effect of surface preparation, Mater. Sci. Eng. C 32 (2012) 1087–1096, https://doi.org/10.1016/j.msec.2011.11.007.

[33] V. Gunther, Y. Yasenchuk, T. Chekalkin, E. Marchenko, S. Gunther, G. Baigonakova, V. Hodorenko, J.H. Kang, S. Weiss, A. Obrosov, Formation of pores and amorphous-nanocrystalline phases in porous TiNi alloys made by self-propagating high-temperature synthesis (SHS), Adv. Powder Technol. 30 (2019) 673–680, https://doi.org/10.1016/j.apt.2018.12.011.

[34] Y. Yasenchuk, V. Gunther, E. Marchenko, T. Chekalkin, G. Baigonakova, V. Hodorenko, S. Gunther, J.H. Kang, S. Weiss, A. Obrosov, Formation of mineral phases in self-propagating high-temperature synthesis (SHS) of porous TiNi alloy, Mater. Res. Express 6 (2019), 056522, https://doi.org/10.1088/2053-1591/ab01a1.

[35] P. Osak, B. Losiewicz, EIS study on interfacial properties of passivated nitinol orthodontic wire in saliva modified with Eludril mouthwash, Protect. Met. Phys. Chem. Surface 54 (2018) 680–688, https://doi.org/10.1134/S2070205118040226.

[36] H. Aihara, J. Zider, G. Fanton, T. Duerig, Combustion synthesis of porous nitinol for biomedical applications, Int. J. Biomater (2019), 4307461, 2019.

[37] J. Schrooten, M. Assad, J. Van Humbeeck, M.A. Leroux, In vitro corrosion resistance of porous NiTi intervertebral fusion devices, Smart Mater. Struct. 16 (2007) 145–154, https://doi.org/10.1088/0964-1726/16/1/S15.

[38] F. Stergioudi, C.A. Vogiatzis, E. Pavlidou, S. Skolianos, N. Michailidis, Corrosion resistance of porous NiTi biomedical alloy in simulated body fluids, Smart Mater. Struct. 25 (2016), 095024, https://doi.org/10.1088/0964-1726/25/9/095024.

[39] X.T. Sun, Z.X. Kang, X.L. Zhang, H.J. Jiang, R.F. Guan, X.P. Zhang, A comparative study on the corrosion behavior of porous and dense NiTi shape memory alloys in NaCl solution, Electrochim. Acta 56 (2011) 6389–6396, https://doi.org/10.1016/j.electacta.2011.05.019.

[40] D. Alferi, V. Hybášek, P. Novák, J. Fojt, Corrosion behaviour of the NiTiX (X = Si, Mg, Al) alloy prepared by self-propagating high-temperature synthesis, Koroze Ochr, Mater 65 (2001) 57–64, https://doi.org/10.2478/kom-2021-0007.

[41] E. Marchenko, G. Baigonakova, K. Dubovikov, Y. Yasenchuk, T. Chekalkin, A. Obrosov, Comparative study on the high- temperature oxidation resistance of porous and solid TiNi-based alloys, Surf. Topogr. Metrol. Prop. 9 (2021) 025007, https://doi.org/10.1088/2051-672X/abf324.

[42] O. Kokorev, T. Chekalkin, E. Marchenko, Y. Yasenchuk, S. Gunther, V. Serebrov, A. Chernyshova, A. Obrosov, E. Uludintceva, J.-H. Kang, Exploring the role of surface modifications of TiNi-based alloys in evaluating in vitro cytocompatibility: a comparative study, Surf. Topogr. Metrol. Prop. 8 (2020) 045015, https://doi.org/10.1088/2051-672X/abc0f9.

[43] E. Marchenko, G. Baigonakova, K. Dubovikov, O. Kokorev, Y. Yasenchuk, A. Vorozhtsov, In vitro bio-testing comparative analysis of NiTi porous alloys modified by heat treatment, Metals 12 (2022) 1006, https://doi.org/10.3390/met12061006.